Radio Science, Volume 25, Number 2, Pages 161–174, March–April 1990

Radial propagation and steepest descent path integral representations of the planar microstrip dyadic Green's function

S. Barkeshli

Sabbagh Associates, Incorporated, Bloomington, Indiana

P. H. Pathak

ElectroScience Laboratory, Department of Electrical Engineering, Ohio State University, Columbus

(Received March 8, 1988; revised November 14, 1989; accepted November 19, 1989.)

A radial propagation integral representation of the microstrip electric dyadic surface Green's function is developed. This representation is very efficient for a numerical evaluation of the field when the source and observation points are laterally rather than vertically separated with respect to the plane of the substrate. Furthermore, when the integration contour is deformed to the steepest descent path, the Green's function exhibits an even faster convergence. In contrast, the conventional Sommerfeld integral representation of the microstrip Green's function converges very poorly for this case. Numerical examples are presented which indicate that the representations obtained here are surprisingly efficient even for relatively small lateral separation of the source and field points. This work is especially useful in the moment method analysis of microstrip antenna arrays where the mutual coupling effects are important.

1. INTRODUCTION

A radial propagation integral representation of the microstrip electric dyadic surface Green's function is developed. The geometry of this microstrip problem is shown in Figure 1. A useful property of this radial propagation Green's function representation is that it is very efficient for a numerical evaluation of the field when the source and observation points are laterally rather than vertically separated with respect to the plane of the substrate. In addition, it is shown that when the contour of integration for this radial propagation representation is deformed into the steepest descent path, then this Green's function exhibits an even faster convergence for lateral separations in excess of the free space wavelength. These radial propagation and steepest descent integral representations of the microstrip Green's functions will allow an efficient moment method (MM) type evaluation of the currents induced on appropriately fed arbitrarily shaped microstrip patch antenna elements (and other types of microstrip circuit elements), when these currents occur as the unknowns within an integral equation whose Kernel is the microstrip Green's function. Such an MM based full wave solution of the integral equation for the microstrip currents automatically includes all mutual coupling effects and radiation losses, etc., which most approximate analyses end up neglecting. It is noted that the conventional exact Sommerfeld integral representation of the microstrip Green's function converges rapidly for source and field points which are vertically (z) separated with respect to the plane of the substrate (see Figure 1); consequently, the conventional Sommerfeld integral representation becomes very poorly convergent when used in this MM solution of the integral equation for the microstrip patch currents, because such an MM analysis generally requires radially or laterally (ρ) separated source and observation points rather than vertically (z) separated with respect to the plane of the substrate. It is for this reason that the present radial propagation integral representation of the microstrip Green's function and also the steepest descent path integral representation serve to substantially improve the computational speed of the MM solution for the currents on the microstrip patch antennas and the microstrip feed lines.

A direct evaluation of the Sommerfeld type integral for the related classical half-space problem has been performed by *Siegel and King* [1970], *Burke and Miller* [1984], *Johnson and Dudley* [1983], and

Paper number 89RS03551.
0048-6604/90/89RS-03551$08.00

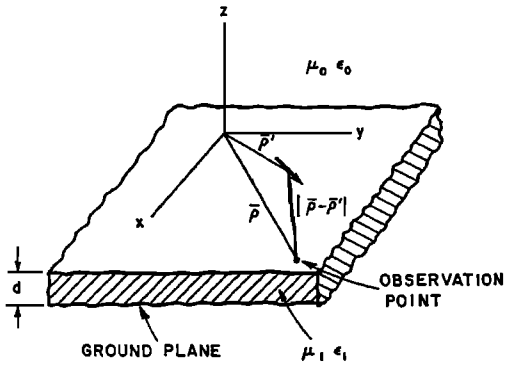

Fig. 1. Geometrical configuration of microstrip dyadic surface Green's function; electric current point source on a grounded planar dielectric slab.

others. On the other hand, the Fast Fourier Transform (FFT) evaluation of the conventional Sommerfeld integral representation for the fields in the half space problem have been employed by *Tsang et al.* [1974] and *Mohsen* [1982]. The integration along the branch cut has been suggested by *Kong et al.* [1977], and the deformation of the original Sommerfeld integral contour into the steepest descent path has also been used to improve the convergence of the Sommerfeld solution for the half-space problem by *Parhami et al.* [1980]; and the latter approach has been further improved by *Michalski* [1985]. In microstrip geometries where the source and observation points are both on the substrate, the evaluation of the conventional Sommerfeld type integral representation for the microstrip Green's function becomes very inefficient as mentioned earlier, because of the absence of the exponential decay of the integrand which occurs only for vertically separated source and field points in that representation.

A combination of numerical and analytical treatment of the conventional Sommerfeld integral representation for the microstrip Green's function has been proposed by *Rana and Alexopoulos* [1981] and by *Katehi and Alexopoulos* [1983] to somewhat alleviate the poor convergence problem with this representation. In addition, an asymptotic extraction technique has also been proposed by *Barkeshli and Pathak* [1986], *Jackson and Alexopoulos* [1986] and *Mosig and Sarkar* [1986] to accelerate the convergence of the conventional Sommerfeld integral representation of the microstrip surface Green's function. It is noted that the asymptotic extraction technique can indeed be utilized to some extent to efficiently evaluate the microstrip dyadic Green's function. Nevertheless, as the lateral separation between the source and observation points increases, the usual Sommerfeld integrand starts to oscillate rapidly. These oscillations are due to the rapid growth of the argument of the Bessel function in the integrand which causes the asymptotic extraction method to eventually lose its efficiency [*Barkeshli*, 1988]. *Mosig and Gardiol* [1982, 1983] perform a deformation of the original Sommerfeld contour of integration to evaluate the otherwise highly oscillatory Sommerfeld integrals. The present approach described here for obtaining an alternative radial propagation representation of the microstrip dyadic Green's function for the special case of a lossless dielectric substrate reduces to expressions to those given by *Mosig and Gardiol* [1982, 1983]; however, the formal radial propagation integral representation is developed here by a different and very direct procedure, it is quite general and unlike the method proposed by Mosig and Gardiol, can be applied to lossy dielectric substrates. Furthermore, when the integration contour of the formal radial propagation representation of the microstrip dyadic Green's function is deformed to the steepest descent path, an even more efficient integral representation of the Green's function will result for source and observation points separated in excess of a free space wavelength. Recently, *Mosig and Sarkar* [1986] have studied the problem of a horizontal dipole above a lossy dielectric substrate. It is claimed in that study that the integration of the Sommerfeld integral along the real axis is always most efficient. However in their analysis, in order to smooth the sharply discontinuous nature of the original Sommerfeld integrand in the vicinity of the branch point, two angular spectrum transformations have been performed which mathematically is not a real axis Sommerfeld integration. It is also interesting to note that the formal radial propagation representation presented here leads to an efficient approximate closed form asymptotic representation of the microstrip dyadic Green's function [*Barkeshli and Pathak*, 1986; *Barkeshli*, 1988; *Barkeshli et al.*, 1990] which also remains accurate even for very small lateral separation of the source and fields points; this relatively simple closed form result will be reported separately.

The format of this paper is as follows. Section 2 deals with the formulation of the microstrip Green's

function which leads to the conventional Sommerfeld integral representation for this case; as indicated earlier, such a representation is poorly convergent for laterally instead of vertically separated source and field points. The alternative radial propagation integral representation of the microstrip dyadic Green's function which is found to remain very efficient for small, to moderately large lateral separation of source and field points ($0.5\lambda_0$ to $4.0\lambda_0$) is derived in section 3.1. A deformation of the contour of integration for the representation obtained in section 3.1 into the steepest descent path (SDP) is derived next in section 3.2 such that it is efficient for lateral separation of the source and field points in excess of a free space wavelength. Section 4 deals with the numerical results; special attention is devoted to the convergence behavior of these different alternative representations for the dyadic microstrip Green's function.

2. FORMULATION OF THE CONVENTIONAL SOMMERFELD REPRESENTATION FOR THE MICROSTRIP GREEN'S FUNCTION

Consider an arbitrarily oriented electric current source $\mathbf{J}(\mathbf{r}')$ in free space radiating in the presence of a grounded dielectric slab. In this configuration, the medium (0) refers to free space with constitutive parameters μ_0, ε_0, and medium (1) corresponds to the grounded dielectric slab with constitutive parameters μ_1, ε_1, and thickness d. The electric field $\mathbf{E}_m$ ($m = 0$ or 1) for this microstrip geometry can be related to the microstrip dyadic Green's function $\mathcal{G}^m(\mathbf{r}, \mathbf{r}')$ [*Tai*, 1971],

$$\mathbf{E}_m = -j\omega\mu_0 \iiint_v \mathcal{G}^m(\mathbf{r}, \mathbf{r}') \cdot \mathbf{J}(\mathbf{r}')\, dv' \tag{1}$$

If the electric current density $\mathbf{J}(\mathbf{r}')$ is taken to be a point source of strength $\mathbf{p}_e$ at $r = r'$

$$\mathbf{J}(\mathbf{r}') = \mathbf{p}_e \delta(\mathbf{r} - \mathbf{r}') \qquad \mathbf{p}_e = p_{ex}\hat{x} + p_{ey}\hat{y} + p_{ez}\hat{z} \tag{2}$$

in which $\delta(\mathbf{r} - \mathbf{r}')$ is the Dirac delta function, then the electric field $\mathbf{E}_m$ produced by $\mathbf{p}_e$ is given as,

$$\mathbf{E}_m = -j\omega\mu_0 \mathcal{G}^m(\mathbf{r}, \mathbf{r}') \cdot \mathbf{p}_e \tag{3}$$

For microstrip geometries the point source $\mathbf{p}_e$ is transverse to $\hat{z}$ (i.e. parallel to the plane of the dielectric slab) and typically lies on the dielectric interface at ($z' = 0$), (see Figure 1). A more convenient matrix form of the above equation is given by,

$$\begin{bmatrix} E_{mx} \\ E_{my} \\ E_{mz} \end{bmatrix} = -j\omega\mu_0 \begin{bmatrix} \mathcal{G}^m_{xx} & \mathcal{G}^m_{xy} & \mathcal{G}^m_{xz} \\ \mathcal{G}^m_{yx} & \mathcal{G}^m_{yy} & \mathcal{G}^m_{yz} \\ \mathcal{G}^m_{zx} & \mathcal{G}^m_{zy} & \mathcal{G}^m_{zz} \end{bmatrix} \begin{bmatrix} p_{ex} \\ p_{ey} \\ 0 \end{bmatrix} \tag{4}$$

with the $\mathbf{p}_e$ now defined as,

$$\mathbf{p}_e \equiv p_{ex}\hat{x} + p_{ey}\hat{y} \qquad (p_{ez} = 0 \text{ here}) \tag{5}$$

One identifies the following elements of $\mathcal{G}_m$ as [*Barkeshli and Pathak*, 1986; *Barkeshli*, 1988]:

$$\mathcal{G}^m_{xx}(\mathbf{r}, \mathbf{r}') = -\frac{1}{j\omega\mu_0} \cdot \left[\nabla_t^2 G''_m - \frac{\partial^2}{\partial x^2}\left(G''_m + \frac{1}{j\omega\varepsilon_m}\frac{1}{j\omega\varepsilon_0}\frac{\partial^2}{\partial z \partial z'} G'_m\right)\right] \tag{6}$$

$$\mathcal{G}^m_{yx}(\mathbf{r}, \mathbf{r}') = -\frac{1}{j\omega\mu_0} \cdot \left[-\frac{\partial}{\partial x}\frac{\partial}{\partial y}\left(G''_m + \frac{1}{j\omega\varepsilon_m}\frac{1}{j\omega\varepsilon_0}\frac{\partial^2}{\partial z \partial z'} G'_m\right)\right] \tag{7}$$

$$\mathcal{G}^m_{zx}(\mathbf{r}, \mathbf{r}') = -\frac{1}{j\omega\mu_0}\left[\frac{1}{j\omega\varepsilon_m}\frac{1}{j\omega\varepsilon_0}\frac{\partial^2}{\partial x \partial z'} \nabla_t^2 G'_m\right] \tag{8}$$

$$\mathcal{G}^m_{xy}(\mathbf{r}, \mathbf{r}') = \mathcal{G}^m_{yx}(\mathbf{r}, \mathbf{r}') \tag{9}$$

$$\mathcal{G}^m_{yy}(\mathbf{r}, \mathbf{r}') = -\frac{1}{j\omega\mu_0} \cdot \left[\nabla_t^2 G''_m - \frac{\partial^2}{\partial y^2}\left(G''_m + \frac{1}{j\omega\varepsilon_m}\frac{1}{j\omega\varepsilon_0}\frac{\partial^2}{\partial z \partial z'} G'_m\right)\right] \tag{10}$$

$$\mathcal{G}^m_{zy}(\mathbf{r}, \mathbf{r}') = -\frac{1}{j\omega\mu_0}\left[\frac{1}{j\omega\varepsilon_m}\frac{1}{j\omega\varepsilon_0}\frac{\partial^2}{\partial y \partial z'} \nabla_t^2 G'_m\right] \tag{11}$$

where

$$G_m = \frac{1}{2\pi}\int_0^\infty g_m(\xi, z, z')\frac{J_0(\xi\rho)}{\xi}\, d\xi \qquad \rho = |\bar{\rho} - \bar{\rho}'| \tag{12}$$

and

$$\nabla_t^2 G_m = -\frac{1}{2\pi}\int_0^\infty g_m(\xi, z, z') J_0(\xi\rho)\xi\, d\xi \tag{13}$$

and the prime (') and double prime ('') symbols have been omitted for convenience. The (∇_t^2) operator is defined as a transverse Del square operator (i.e.,

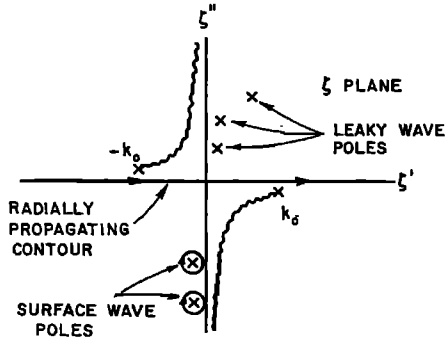

Fig. 4. Complex ζ plane and the real axis contour of integration of (27).

$$\nabla_t^2 G_m = \frac{-1}{4\pi}\left[\int_{C_B} g_m(\xi, z, z') H_0^{(2)}(\xi\rho)\xi\, d\xi - 2\pi j \sum_{p=1}^{N} Res(g_m(\xi_p, z, z'))\xi_p H_0^{(2)}(\xi_p\rho)\right] \tag{24}$$

where the finite sum refers to the discrete spectral or pole wave contribution to $\nabla_t^2 G_m$ and the integral of C_B is the continuous spectral contribution to $\nabla_t^2 G_m$; also, the *Res* is defined as the residue of g_m at the poles $\xi = \xi_p$; i.e.

$$Res(g_m(\xi_p, z, z')) = \lim_{\xi \to \xi_p} (\xi - \xi_p) g_m(\xi, z, z') \tag{25}$$

The integral contour C_B can be transformed to the real axis by introducing the change of variable [*Felsen and Marcuvitz*, 1973],

$$\zeta = -\sqrt{k_0^2 - \xi^2} \qquad d\xi = \frac{-\zeta d\zeta}{\sqrt{k_0^2 - \zeta^2}} \tag{26}$$

It is noted that as ξ varies along the contour C_B of the Figure 3, the new variable of integration ζ will vary from $+\infty$ to $-\infty$ along the real ζ axis as shown in Figure 4. Note that the circular contour which encircles the branch point does not contribute. Finally, one obtains (see Figures 3 and 4),

$$\nabla_t^2 G_m = \frac{-1}{4\pi}\left[\int_{-\infty}^{\infty} g_m(\zeta, z, z') H_0^{(2)}(\rho\sqrt{k_0^2 - \zeta^2})\zeta\, d\zeta - 2\pi j\left(\sum_p Res(g_m(\xi_p, z, z))\xi_p H_0^{(2)}(\xi_p\rho)\right)\right] \tag{27}$$

The above result in (27) represents the alternative ρ-propagation representation of $\nabla_t^2 G_m$ which is obtained from its Sommerfeld representation in (22).

The radial propagation planar microstrip dyadic Green's function for $z = z' = 0$, can be constructed after incorporating $(\nabla_t^2 G_0'')$, $[(\partial/\partial z')\nabla_t^2 G_0']$ and $\{G_0'' - [1/(\omega\varepsilon_0)^2](\partial^2/\partial z \partial z')G_0'\}$ given in the following into (6)–(11),

$$\nabla_t^2 G_0'' = \frac{-1}{4\pi}\left(\frac{k_0^2}{\omega\varepsilon_0}\int_{-\infty}^{\infty} \frac{H_0^{(2)}(\rho\sqrt{k_0^2 - \zeta^2})\zeta}{\zeta + k_0 Y(\zeta)}\, d\zeta - 2\pi j \sum_{p''=1}^{N''} Res(g_0''(\xi_{p''}, 0, 0))\xi_{p''} H_0^{(2)}(\xi_{p''}\rho)\right) \tag{28}$$

$$\frac{\partial}{\partial z'}\nabla_t^2 G_0' = \frac{-1}{4\pi} \cdot \left[\frac{k_0^2}{\omega\mu_0}\int_{-\infty}^{\infty} \frac{-jk_0 Z(\zeta)}{\zeta + k_0 Z(\zeta)} H_0^{(2)}(\rho\sqrt{k_0^2 - \zeta^2})\zeta\, d\zeta - 2\pi j \sum_{p'=1}^{N'} \frac{\partial}{\partial z'} Res(g_0'(\xi_{p'}, z, z'))\zeta_{p'} H_0^{(2)}(\xi_{p'}\rho)\Big|_{z=z'=0}\right] \tag{29}$$

and

$$\left(G_0'' - \frac{1}{(\omega\varepsilon_0)^2}\frac{\partial^2}{\partial z \partial z'} G_0'\right) = \frac{1}{4\pi}\left\{\frac{1}{\omega\varepsilon_0}\int_{-\infty}^{\infty} \frac{H_0^{(2)}(\rho\sqrt{k_0^2 - \zeta^2})\zeta}{\zeta + k_0 Y(\zeta)} \cdot \left(1 - \frac{\mu_r\varepsilon_r - 1}{\mu_r\varepsilon_r}\frac{\zeta}{\zeta + k_0 Z(\zeta)}\right) d\zeta - 2\pi j\left(\sum_{p''=1}^{N''} Res(g_0''(\xi_{p''}, 0, 0))\frac{H_0^{(2)}(\xi_{p''}\rho)}{\xi_{p''}} + \sum_{p'=1}^{N'} \frac{j\sqrt{k_0^2 - \xi_{p'}^2}}{(\omega\varepsilon_0)^2} \cdot \frac{\partial}{\partial z'} Res(g_0'(\xi_{p'}, z, z'))\frac{H_0^{(2)}(\xi_{p'}\rho)}{\xi_{p'}}\Big|_{z=z'=0}\right)\right\} \tag{30}$$

where

$$Z(\zeta) = \frac{j\kappa_1(\zeta)}{k_0 \varepsilon_r} \tan(d\kappa_1(\zeta)) \tag{31}$$

$$Y(\zeta) = \frac{-j\kappa_1(\zeta)}{k_0 \mu_r} \cot(d\kappa_1(\zeta)) \tag{32}$$

and

$$\kappa_1(\zeta) = \sqrt{(\mu_r \varepsilon_r - 1)k_0^2 + \zeta^2} \tag{33}$$

In the above formulations $z = z' = 0$, (the source and the observation points both lie on the slab) as shown in Figure 1.

One can now see that the radial propagation representation of the planar microstrip dyadic Green's function exhibits fast convergence for laterally separated source and field points. This is due to the fact that for the $\zeta > k_0$, the Hankel functions associated with the integrand in (28)–(30) decay exponentially. Therefore it is more efficient to utilize this representation for the microstrip and related geometries when dealing with an MM solution for the currents on these microstrip configurations. The logarithmic singularity of the Hankel function at $\zeta = \pm k_0$ can be removed via the following transformations;

$$\zeta = k_0\sqrt{1 - \xi^2} \qquad |\zeta| < k_0 \tag{34}$$

and

$$\zeta = k_0\sqrt{1 + \xi^2} \qquad |\zeta| > k_0 \tag{35}$$

therefore the actual form of (28) through (30), which are ultimately being used, are as follows:

$$\nabla_t^2 G_0'' = \frac{-1}{4\pi}\left\{\frac{k_0^3}{\omega\varepsilon_0}\left[\int_0^1 H_0^{(2)}(k_0\rho\xi)\xi \cdot \frac{2\sqrt{1-\xi^2}}{(1-\xi^2) - Y^2(\zeta)}\, d\xi\right|_{\zeta^2 = k_0^2(1-\xi^2)} + \int_0^\infty H_0^{(2)}(-jk_0\rho\xi)\frac{2\sqrt{1+\xi^2}}{(1+\xi^2) - Y^2(\zeta)}\, d\xi\Bigg|_{\zeta^2 = k_0^2(1+\xi k^2)}\Bigg] - 2\pi j \sum_{p''}^{N''} Res(g_0''(\xi_{p''}, 0, 0))\xi_{p''} H_0^{(2)}(\xi_{p''}\rho)\right\} \tag{36}$$

$$\frac{\partial}{\partial z'}\nabla_t^2 G_0' = \frac{-1}{4\pi}\left\{\frac{k_0^3}{\omega\mu_0}\left[\int_0^1 H_0^{(2)}(k_0\rho\xi)\xi \cdot \frac{-jZ(\zeta)2\sqrt{1-\xi^2}}{(1-\xi^2) - Z^2(\zeta)}\, d\xi\right|_{\zeta^2 = k_0^2(1-\xi^2)} + \int_0^\infty H_0^{(2)}(-jk_0\rho\xi)\xi \cdot \frac{-jZ(\zeta)2\sqrt{1+\xi^2}}{(1+\xi^2) - Z^2(\zeta)}\, d\xi\Bigg|_{\zeta^2 = k_0^2(1+\xi^2)}\Bigg] - 2\pi j \cdot \sum_{p'=1}^{N'} \frac{\partial}{\partial z'} Res(g_0'(\xi_{p'}, z, z'))\xi_{p'} H_0^{(2)}(\xi_{p'}\rho)|_{z=z'=0}\right\} \tag{37}$$

$$\left(G_0'' - \frac{1}{(\omega\varepsilon_0)^2}\frac{\partial^2}{\partial z \partial z'} G_0'\right) = \frac{1}{4\pi}\left\{\frac{k_0}{\omega\varepsilon_0}\left[\int_0^1 H_0^{(2)}(k_0\rho\xi)Q_1(\xi)\, d\xi + \int_0^\infty H_0^{(2)}(-jk_0\rho\xi)Q_2(\xi)\, d\xi\right] - 2\pi j\left(\sum_{p''=1}^{N''} Res(g_0''(\xi_{p''}, 0, 0))\frac{H_0^{(2)}(\xi_{p''}\rho)}{\xi_{p''}''} + \sum_{p'=1}^{N'} \frac{j\sqrt{k_0^2 - \xi_{p'}^2}}{(\omega\varepsilon_0)^2}\frac{\partial}{\partial z'} \cdot Res(g_0'(\xi_{p'}, z, z'))\frac{H_0^{(2)}(\xi_{p'}\rho)}{\xi_{p'}}\Bigg|_{z=z'=0}\right)\right\} \tag{38}$$

where

$$Q_1(\xi) = \frac{2\xi\sqrt{1-\xi^2}}{1 - \xi^2 - Y^2(\zeta)} \cdot \left(1 - \frac{\mu_r\varepsilon_r - 1}{\mu_r\varepsilon_r}\frac{1 - \xi^2 + Y(\zeta)Z(\zeta)}{1 - \xi^2 - Z^2(\zeta)}\right)\Bigg|_{\zeta^2 = k_0^2(1-\xi^2)} \tag{39}$$

and

$$Q_2(\xi) = \frac{2\xi\sqrt{1+\xi^2}}{1+\xi^2-Y^2(\zeta)} \cdot \left(1 - \frac{\mu_r\varepsilon_r - 1}{\mu_r\varepsilon_r}\frac{1+\xi^2+Y(\zeta)Z(\zeta)}{1+\xi^2-Z^2(\zeta)}\right)\Bigg|_{\zeta^2 = k_0^2(1+\xi^2)} \tag{40}$$

3.2. *Steepest descent path (SDP) representation of the microstrip Green's function*

This method deals with the deformation of the original contour for the radial propagation representation of the microstrip surface Green's function (obtained in section 3.1) into its steepest descent path (SDP) of integration. It is a technique which allows numerical integration to be employed over the SDP on which the integrand decays most rapidly. In this case, as the separation between the source and observation point increases, the numerical integration becomes even faster and easier to perform.

Consider the integral of the general form

$$I = \int_{-\infty}^{\infty} F(\zeta) H_0^{(2)}(\rho\sqrt{k_0^2 - \zeta^2}) e^{-j\zeta z}\, d\zeta \tag{41}$$

where I can be a typical expression for the integrals occurring in $\nabla_t^2 G_m''$ or $\nabla_t^2 G_m'$. Let's assume for the time being that $k_0\rho \gg 1$, and the use of the large argument asymptotic form of the Hankel function is permissible. Then with a change of variable ($\zeta = k_0\eta$), one will have,

$$I \sim k_0 \int_{-\infty}^{\infty} F(\eta)\sqrt{\frac{2}{\pi k_0\rho\sqrt{1-\eta^2}}} \cdot e^{+j(\pi/4)} e^{-jk_0(\rho\sqrt{1-\eta^2} + z\eta)}\, d\eta \tag{42}$$

Although the saddle point and the steepest descent path can be directly found in the complex η plane, we will perform the angular spectrum mapping for convenience. Thus, let

$$\eta = \cos\gamma \qquad d\eta = -\sin\gamma\, d\gamma \qquad \sqrt{1-\eta^2} = \sin\gamma \tag{43}$$

then,

$$I \sim k_0 \int_{\Gamma} F(\gamma)\sqrt{\frac{2}{\pi\, k_0 \sin\gamma}} \cdot e^{+j(\pi/4)} e^{-jk_0 r\cos(\theta-\gamma)}(\sin\gamma)\, d\gamma \tag{44}$$

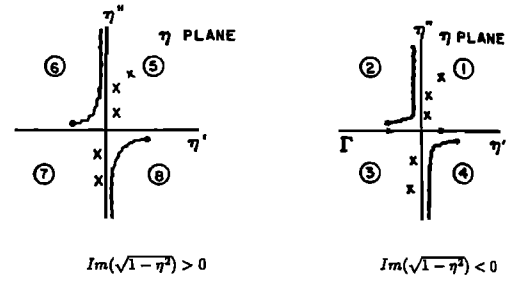

Fig. 5. Two sheeted η plane. First sheet, Im $(1-\eta^2)^{1/2} < 0$; and the second sheet, Im $(1-\eta^2)^{1/2} > 0$.

where

$$\rho = r\sin\theta \quad z = r\cos\theta \quad \tan\theta = \frac{\rho}{z} \tag{45}$$

The integrand exhibits a saddle point a $\gamma_s = \theta$. Let

$$q(\gamma) = -j\cos(\theta - \gamma) \tag{46}$$

Then,

$$q'(\gamma) = j\sin(\theta-\gamma) \quad \gamma_s = \theta \text{ (saddle pt.)} \quad q(\gamma_s) = -j \tag{47}$$

Figures 5 and 6 show the double sheeted η and complex γ planes respectively, with the original path Γ and steepest descent path Γ_{SDP} depicted in the complex γ plane. Note that the steepest descent path is the path on which the following condition holds,

$$Im(q(\gamma)) = Im(q(\gamma_s)) \qquad Re(\cos(\theta-\gamma)) = 1 \tag{48}$$

so

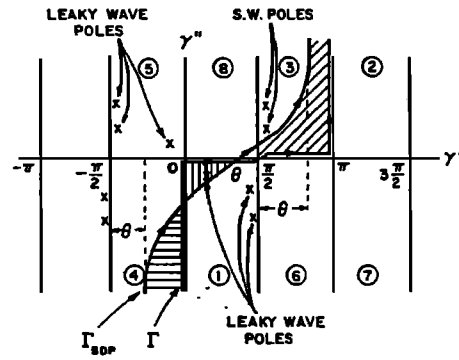

Fig. 6. Angular spectrum mapping where $\eta = \cos\gamma$; the leaky and surface wave poles and the contour of integration Γ and Γ_{SDP}.

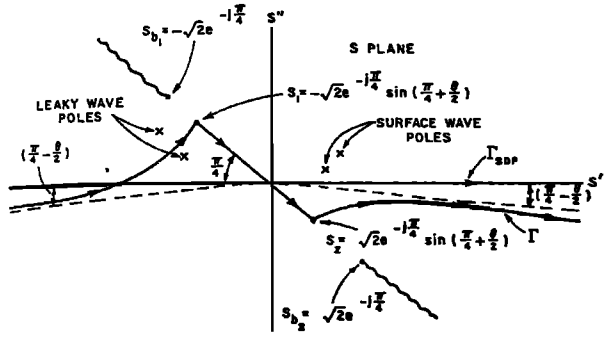

Fig. 7. Complex s plane, original path Γ maps on solid curve, the SDP maps onto the real axis ($-\infty < s < -\infty$), the saddle point $\gamma_s = \theta$, and branch points at $s_{b_{12}} = \pm 2^{1/2} e^{-j\pi/4}[(s^2 + 2j)^{1/2} = 0]$.

$$I \sim k_0 \int_{\Gamma_{SDP}} F(\gamma) \sqrt{\frac{1}{\pi k_0 \rho \sin \gamma}} \cdot e^{+j(\pi/4)} e^{-jk_0 r \cos(\theta - \gamma)} (\sin \gamma)\, d\gamma + 2\pi j \sum_s Res(I(\gamma_s)) - 2\pi j \sum_l Res(I(\gamma_l)) \tag{49}$$

where Γ_{SDP} is the SDP contour, and the summation terms of s and l, stand for the residue contributions arising from the presence of the surface wave and leaky wave poles respectively which may be intercepted during the path deformation. It is noted that unless $\theta \approx (\pi/2)$ ($k_0\rho \gg 1$; $k_0 z \ll 1$), there exists the possibility of crossing one or more of those surface wave poles which are closest to the Real γ axis (see Figure 6) which have been captured during the derivation of ρ-propagation representation (see (27)). This results in the cancellation of some of the surface wave residue contributions in the sum on the right hand side of (27). It is also noted that the same SDP will result if one starts form the Sommerfeld representation (rather than the ρ-propagation representation) since only one SDP exists in each strip of 2π radians in the γ plane, but in this case, the surface wave poles must be found in γ plane. In the following we will map the SDP onto a contour along the real axis in the new complex plane s defined by

$$q(\gamma) - q(\gamma_s) = s^2 \qquad \cos(\theta - \gamma) = 1 - js^2 \tag{50}$$

or

$$\frac{d\gamma}{ds} = \frac{2j}{\sqrt{s^2 + 2j}} \tag{51}$$

with branch points at $(s^2 + 2j)^{1/2} = 0$. This transformation maps the steepest descent path Γ_{SDP}, on the real axis of the complex s plane as indicated above. The saddle point at $\gamma_s = \theta$ is now mapped to $s = 0$ (see Figure 7). For the $\theta = \pi/2$ the source and the observation points lie on the interface (i.e., $k_0 z = 0$), one will have

$$\sin \gamma = 1 - js^2 \qquad \cos \gamma = |s| \sqrt{s^2 + 2j} \tag{52}$$

and

$$H_0^{(2)}(k_0 \rho \sin \gamma) = H_0^{(2)}(k_0 \rho (1 - js^2)) \tag{53}$$

therefore the SDP representation of I in the s plane will be

$$I = k_0 \int_{-\infty}^{\infty} F(s) H_0^{(2)}(k_0 \rho (1 - js^2)) \frac{2j(1 - js^2)}{\sqrt{s^2 + 2j}}\, ds - 2\pi j \sum_l Res(I(\gamma_l)) \tag{54}$$

Note that for the particular case of $\theta = \pi/2$ (i.e., both source and observation points on the substrate) no surface wave pole will be intercepted during the path deformation. The final SDP representation for microstrip dyadic surface Green's function which is suitable for numerical integration can be found from (6)–(11) and the following results with $z = z' = 0$ (the source and observation located on the slab) as shown in Figure 1:

$$\nabla_t^2 G_0'' = -\frac{1}{4\pi} \left[\frac{4k_0^3}{\omega \varepsilon_0} \int_0^{\infty} H_0^{(2)}(k_0 \rho (1 - js^2)) F_1(s)\, ds - 2\pi j \sum_{p''=1}^{N''} Res(g_0''(\xi_{p''}, 0, 0)) \xi_{p''} H_0^{(2)}(\xi_{p''} \rho) \right] \tag{55}$$

$$\frac{\partial}{\partial z'} \nabla_t^2 G_0' = -\frac{1}{4\pi} \left[\frac{4k_0^3}{\omega \mu_0} \int_0^{\infty} H_0^{(2)}(k_0 \rho (1 - js^2)) F_2(s)\, ds - 2\pi j \sum_{p'=1}^{N'} \frac{\partial}{\partial z'} \cdot Res(g_0'(\xi_{p'}, z, z')) \xi_{p'} H_0^{(2)}(\xi_{p'} \rho)\big|_{z=z'=0} \right] \tag{56}$$

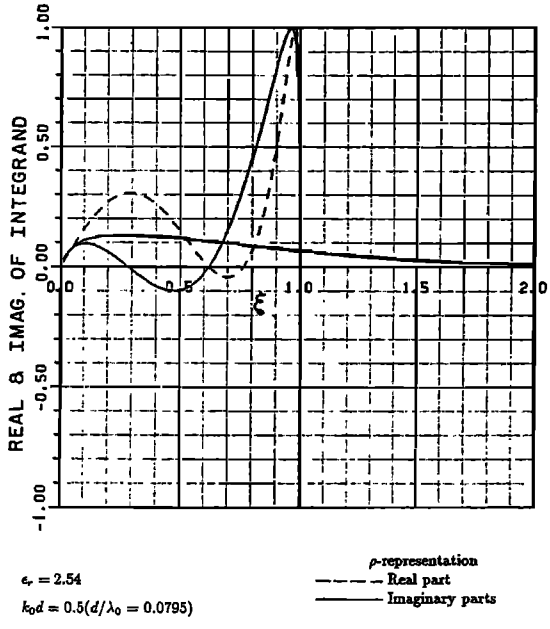

Fig. 8a

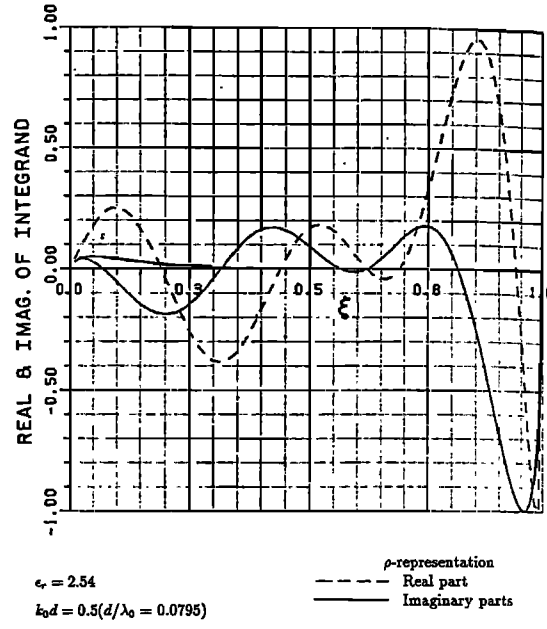

Fig. 8b

Fig. 8. (*a*) Integrand of $\{G_0'' - [1/(\omega\varepsilon_0)^2](\partial^2/\partial z\partial z')G_0'\}$ in equation (38) versus ξ for $\rho = 0.5\lambda_0$. (*b*) Integrand of $\{G_0'' - [1/(\omega\varepsilon_0)^2](\partial^2/\partial z\partial z')G_0'\}$ in equation (38) versus ξ for $\rho = 2.\lambda_0$.

$$G_0'' - \frac{1}{(\omega\varepsilon_0)^2}\frac{\partial^2}{\partial z\partial z'}G_0' = \frac{1}{4\pi}\left[\frac{4k_0}{\omega\varepsilon_0}\int_0^\infty H_0^{(2)}(k_0\rho(1-js^2))F_3(s)\,ds - 2\pi j\left(\sum_{p''=1}^{N''} Res(g''(\xi_{p''}, 0, 0))\frac{H_0^{(2)}(\xi_{p''}\rho)}{\xi_{p''}} + \sum_{p'=1}^{N'}\frac{j\sqrt{k_0^2-\xi_p^2}}{(\omega\varepsilon_0)^2}\frac{\partial}{\partial z'}\cdot Res(g'(\xi_{p'}, z, z'))\xi_{p'}H_0^{(2)}(\xi_{p'}\rho)|_{z=z'=0}\right)\right] \quad (57)$$

where

$$F_1(s) = \frac{(s^2+j)s^2\sqrt{s^2+2j}}{s^2(s^2+2j) - Y^2(s)} \quad (58)$$

$$F_2(s) = \frac{(s^2+j)s^2\sqrt{s^2+2j}(-jZ(s))}{s^2(s^2+2j) - Z^2(s)} \quad (59)$$

$$F_3(s) = \frac{s^2+js^2\sqrt{s^2+2j}}{s^2(s^2+2j) - Y^2(s)} \cdot\left(1 - \frac{\mu_r\varepsilon_r - 1}{\mu_r\varepsilon_r}\frac{s^2(s^2+2j) - Y(s)Z(s)}{s^2(s^2+2j) - Z^2(s)}\right) \quad (60)$$

and

$$Y(s) = -j\sqrt{(\mu_r\varepsilon_r - 1) + s^2(s^2+2j)} \cdot\frac{\cot k_0 d\sqrt{(\mu_r\varepsilon_r - 1) + s^2(s^2+2j)}}{\mu_r} \quad (61)$$

$$Z(s) = j\sqrt{(\mu_r\varepsilon_r - 1) + s^2(s^2+2j)} \cdot\frac{\tan k_0 d\sqrt{(\mu_r\varepsilon_r - 1) + s^2(s^2+2j)}}{\varepsilon_r} \quad (62)$$

If the leaky wave poles are excited, the contribution of these poles must also be added to the integrals given in (55)–(57) as it is evident from (54).

4. NUMERICAL RESULTS

In this section, the integrands of the $\{G_0'' - [1/(\omega\varepsilon_0)^2](\partial^2/\partial z\partial z')G_0'\}$ in (38) and (57) will be stud-

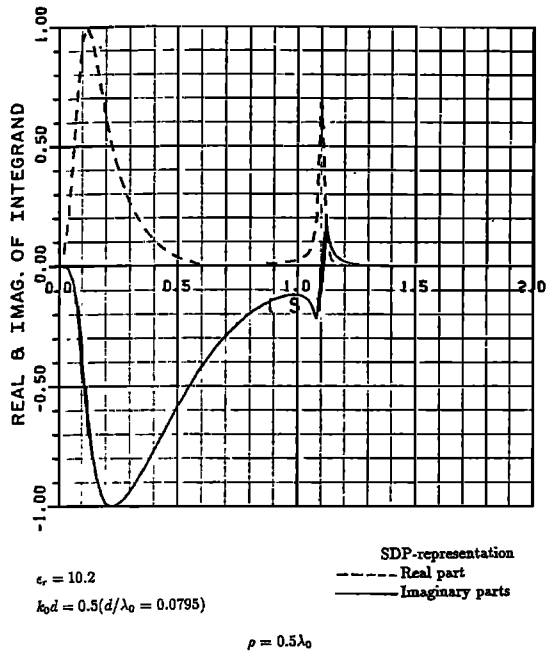

Fig. 9a

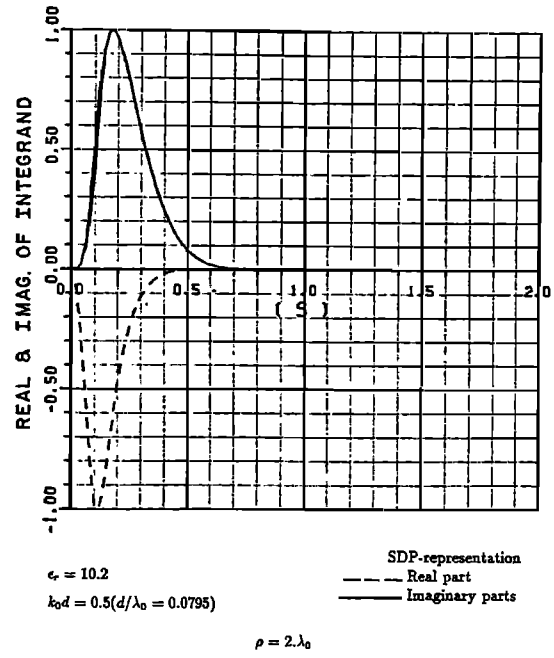

Fig. 9b

Fig. 9. (*a*) Integrand of $\{G_0'' - [1/(\omega\varepsilon_0)^2](\partial^2/\partial z \partial z')G_0'\}$ in equation (57) versus s for $\rho = 0.5\lambda_0$. (*b*) Integrand of $\{G_0'' - [1/(\omega\varepsilon_0)^2](\partial^2/\partial z \partial z')G_0'\}$ in equation (57) versus s for $\rho = 2.\lambda_0$.

ied. The behavior of the integrands of $\nabla_t^2 G_0''$ in (36) and (55), and $(\partial/\partial z')\nabla_t^2 G_0'$ in (37) and (56) follow the same patterns as those that will be presented here.

Figures 8*a* and 8*b* show a typical behavior of the integrand of $\{G_0'' - [1/(\omega\varepsilon_0)^2](\partial^2/\partial z \partial z')G_0'\}$ in Equation (38) as the function of its argument ξ for a single layer microstrip configuration with a dielectric constant $\varepsilon_r = 2.54$ and of thickness equal to $0.0795\lambda_0$ when the lateral distances are $\rho = 0.5\lambda_0$ and $2.0\lambda_0$ respectively. It is important to note that the real part of this integral always exists over finite limits that have their end points at 0 and 1; whereas, the imaginary part which exists over semi-infinite limits is always exponentially decaying as the function of the argument. As the lateral separation between the source and observation points increases, the infinite integral decays faster, but the number of oscillations in the finite integrals increases. This can be seen from Figure 8*b* when $\rho = 2.0\lambda_0$. These oscillations are due to the behavior of the Hankel function as its argument becomes larger. It is interesting to note that in the Sommerfeld representation, the total number of oscillations of the integrand between 0 and 1 of its semi-infinite interval of integration are the same as the number of oscillations of the integrand of the radial propagation representation which exists only over finite limits from 0 to 1. Over the rest of the interval of integration from 1 to infinity, however, the Sommerfeld integrand exhibits an infinite number of oscillations; no such oscillations exist for the radial propagation representation. The advantage of the radial propagation representation against the conventional Sommerfeld representation is now apparent. The next figures deal with the numerical results based on the steepest descent path (SDP) representation. Figures 9*a* and 9*b* depict the integrand of the SDP representation of $(G_0'' - [1/(\omega\varepsilon_0)^2](\partial^2/\partial z \partial z')G_0')$ given in Equation (57) versus its argument(s) for slab thickness of $0.0795\lambda_0$ with the dielectric constant $\varepsilon_r = 10.2$. Unlike the previous cases, the integrands now become smoother as the lateral separation between the source and observation points increases; therefore, they will be easier to evaluate. Nevertheless, for small lateral separations, a numerical irregularity appears in the integrand of the SDP representation (Figure 9*a*). These irregularities, and rapid changes in the integrand for the case in Figure 9*a* are mostly due to the unexcited leaky wave pole (not being captured by SDP in this instance) which is very close to the SDP path. One can use the following procedure to avoid these irregularities

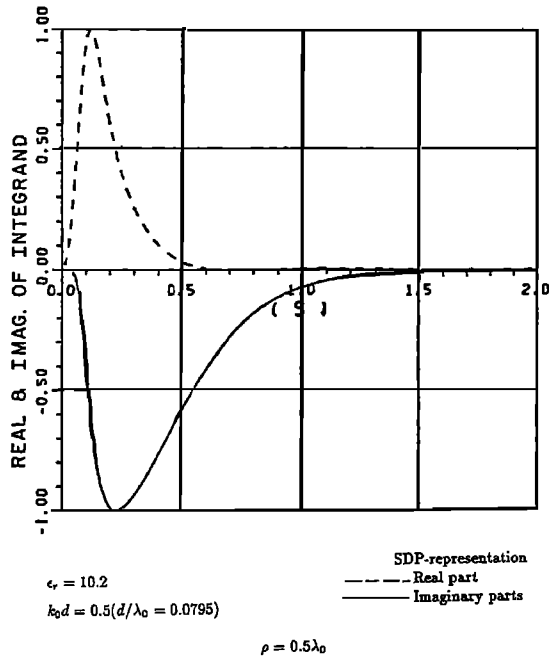

Fig. 10. Integrand of $\{G_0'' - [1/(\omega\varepsilon_0)^2](\partial^2/\partial z \partial z')G_0'\}$ in equation (57) versus s with close by leaky wave singularity extracted; for $\rho = 0.5\lambda_0$.

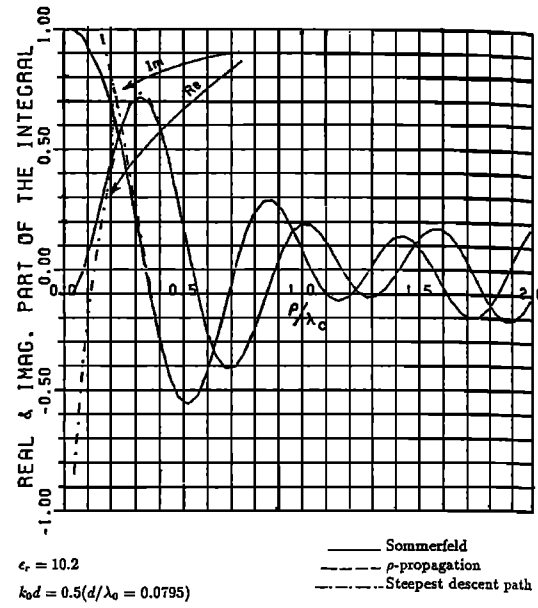

Fig. 11. Typical value of $\{G_0'' - [1/(\omega\varepsilon_0)^2](\partial^2/\partial z \partial z')G_0'\}$ versus ρ/λ_0 from three different representations; Sommerfeld representation, ρ-representation (equation (38)), and SDP representation (equation (57)).

and thereby improve the numerical behavior of the integrand. Let a typical integral of the type being considered by expressed as

$$\int_{s_1}^{s_2} F(s)\,ds = \int_{s_1}^{s_2} \left[F(s) - \frac{Res(s_p)}{s - s_p}\right] ds + Res(s_p)\left(\ln\left|\frac{s_2 - s_p}{s_1 - s_p}\right| + j\,Arg\left(\frac{s_2 - s_p}{s_1 - s_p}\right)\right) \quad (63)$$

where the integrand, given in the bracket is a regular and slow varying function. Figure 10 depicts the same integrand as Figure 9*a* with the leaky wave pole singularity being subtracted. Although the integrand with the singularity subtracted is easier to evaluate as can be seen from the comparison between Figures 9*a* and 10, it is now necessary to find the leaky wave poles via a numerical search technique before these pole effects can be subtracted. However, for moderate size substrate thickness, the inclusion of contributions of leaky wave poles

TABLE 1. Approximate Computational Time in Seconds on an Alliant *FX*/4 Computer

ρ/λ_0	CPU Time for Numerical Integration of Sommerfeld Representation	CPU Time for Numerical Integration of ρ Representation	CPU Time for Numerical Integration SDP Representation
0.25	2.4×10^{-1} s	2.2×10^{-1} s	5.0×10^{-1} s
0.50	2.9×10^{-1} s	1.7×10^{-1} s	4.0×10^{-1} s
1.0	3.8×10^{-1} s	1.2×10^{-1} s	3.5×10^{-1} s
2.0	4.2×10^{-1} s	2.3×10^{-1} s	2.0×10^{-1} s
5.0	8.9×10^{-1} s	3.2×10^{-1} s	1.2×10^{-1} s

Calculation of $\{G_0'' - [1/(\omega\varepsilon_0)^2](\partial^2/\partial z \partial z')G_0'\}$ by numerical integration of Sommerfeld representation, ρ representation of (38), and steepest descent path (SDP) representation of (57), as a function of ρ/λ_0 for a dielectric constant of $\varepsilon_r = 10.2$ and substrate thickness $k_0 d = 0.5(d/\lambda_0 = 0.0795)$.

even when they will be captured by the SDP are not necessary, if one uses the SDP representation for lateral distances from the source point larger than one to two free space wavelengths, as is evident from Figure 9*b*; the main reason why this is so is because the Hankel function with the large complex argument decays faster exponentially for larger lateral separation between source and field points and dominates over any irregularities or any contribution that comes form the nearby singularities; hence, most of the contribution to the integral comes from the vicinity of the saddle point at $s = 0$. Moreover, the residues of the leaky wave poles have their maximum exponential decay in the lateral $\hat{\rho}$ direction. It is noted that, the SDP representation can indeed be used to evaluate the field points arbitrarily close to the source, but the nearby leaky wave poles ought to be determined in this case in order to have an efficient and accurate representation. A careful numerical study reveals that the SDP representation is a more efficient representation than the other ones for lateral source and field point separations as small as $0.5\lambda_0$ if the nearest singularity to the SDP were removed analytically. Finally, Figure 11 shows the typical result of $\{G_0'' - [1/(\omega\varepsilon_0)^2](\partial^2/\partial z \partial z')G_0'\}$ as a function of ρ/λ_0 (for a dielectric constant $\varepsilon_r = 10.2$ and a substrate thickness of $0.0795\lambda_0$), which has been calculated from three different representations; namely, by the Sommerfeld (z propagation) representation; by the radial (ρ-propagation) representation, (38); and by steepest descent path (SDP) representation, (57) respectively. It is apparent from the figure that all three different methods give rise to the same numerical results from the different integral representations (irregularities for small lateral separations of $\rho/\lambda_0 < 0.2$ in the SDP based evaluation are due to the small number of sampling points in the integration routine); nonetheless, as indicated by Table 1, the computational times are very much different for a given achievable accuracy and for a given ρ/λ_0. In this study the numerical integration are performed using Gaussian quadrature for the accuracy up to forth significant figure. For the Sommerfeld representation, the numerical integration is performed after the surface wave pole singularities and the limiting behavior of the integrand have been subtracted; no special integration schemes for the discontinuous nature of the integrand in the branch point or non-linear transformations for the slowly convergent tail of the Sommerfeld integrand [*Mosig and Gardiol*, 1983] have been utilized. For the SDP representation, no nearby leaky wave singularities have been removed. It is concluded that, in general for the very small lateral separations, less than a quarter to half a free space wavelength, the Sommerfeld representation is more efficient; for the relatively small to a moderately large lateral separations, in the range of half to four free space wavelengths, the ρ representation is more efficient, and for lateral separations (larger than one or two free space wavelengths), the SDP representation is the most efficient one. It is to be noted that in all the figures, the values of the integrands are normalized to their absolute maximum, hence all values of the integrand lie between -1.0 and 1.0.

Acknowledgments. This work was supported in part by the Joint Services Electronics program, contract N00014-78-C-0049 and the Ohio State University Research Foundation.

REFERENCES

Barkeshli, S., An efficient approach for evaluating the planar microstrip Green's function and its applications to the analysis of microstrip antennas and arrays, Ph.D. dissertation, Dep. Electr. Eng., Ohio State Univ., Columbus, 1988.

Barkeshli, S., and P. H. Pathak, An efficient approach for evaluating the planar microstrip Green's function, paper presented at the International IEEE Antennas and Propagation Symposium and National Radio Science Meeting, Inst. of Electr. and Electron. Eng., Philadelphia, Pa., June 9–13, 1986.

Barkeshli, S., and P. H. Pathak, "On the dyadic Green's function of the multilayered dielectric/ferrite media," paper presented at the International IEEE Antennas and Propagation Symposium and National Radio Science Meeting, Inst. of Electr. and Electron. Eng., Blacksburg, Va., June 15–19, 1987.

Barkeshli, S., P. H. Pathak, and M. Marin, An asymptotic closed form microstrip surface Green's function for the efficient moment method analysis of mutual coupling in microstrip antennas, *IEEE Trans. Antennas Propag.*, in press, 1990.

Burke, G. J., and E. K. Miller, Modeling antennas near to and penetrating a lossy interface, *IEEE Trans. Antennas Propag.*, *AP-32*, 1040–1049, 1984.

Burke, G. J., E. K. Miller, J. N. Brittingham, D. L. Lager, R. J. Lytle, and J. T. Okada, Computer modeling of antennas near the ground, Electromagn., *1*, 29–49, 1984.

Felsen, L. B., and N. Marcuvitz, Radiation and scattering of waves, chap. 5, Prentice-Hall, Englewood Cliffs, N. J., 1973.

Jackson, D. A., and N. G. Alexopoulos, An asymptotic extraction technique for evaluating sommerfeld-type integrals, *IEEE Trans. Antennas Propag.*, *AP-34*, 1467–1470, 1986.

Johnson, W. A., and D. G. Dudley, Real axis integration of Sommerfeld integrals, source and observation points in air, *Radio Sci.*, *18*, 175–186, 1983.

Katehi, P. B., and N. G. Alexopoulos, Real axis integration of Sommerfeld integrals with application to printed circuit anten-

nas, *J. Math Phys.*, *24*(3), 527–32, 1983.

Kong, J. A., L. C. Shen, and L. Tsang, Field of an antenna submerged in a dissipative dielectric medium, *IEEE Trans. Antennas Propag.*, *AP-25*, 887–889, 1977.

Michalski, K. A., On the efficient evaluation of integrals arising in the Sommerfeld half-space problem, *Proc. Inst. Electr. Eng.*, *32*, 312–318, 1985.

Mohsen, A., On the evaluation of Sommerfeld integrals, *Proc. Inst. Electr. Eng.*, *129*, 177–182, 1982.

Mosig, J. R., and F. E. Gardiol, *A Dynamic Radiation Model for Microstrip Structures in Advanced Electrical and Electron Physics*, vol. 59, Academic Press, San Diego, Calif., 1982.

Mosig, J. R., and F. E. Gardiol, Analytical and numerical techniques in the Green's function treatment of microstrip antennas and scatterers, *Proc. Inst. Electr. Eng.*, *130*, 175–182, 1983.

Mosig, J. R., and T. K. Sarkar, Comparison of quasi-static and exact electromagnetic fields from a horizontal electric dipole above a lossy dielectric backed by an imperfect ground plane, *IEEE Trans. Microwave Theory Tech.*, *MTT-24*(4), 379–387, 1986.

Parhami, P., Y. Rahmat-Sami, and R. Mittra, An efficient approach for evaluating sommerfeld integrals encountered in the problem of a current element radiating over lossy ground, *IEEE Trans. Antennas Propag.*, *AP-18*, 100–104, 1980.

Rana, I. E., and N. G. Alexopoulos, Current distribution and input impedance of printed dipoles, *IEEE Trans. Antennas Propag.*, *AP-29*(1), 99–105, 1981.

Siegel, M., and R. W. P. King, Electromagnatic fields in a dissipative half-space-Anumerical approach, *J. Appl. Phys.*, *41*(6), 2415–2423, 1970.

Tai, C. T., *Dyadic Green's Function in Electromagnetic Theory*, Intext Educational Publishers, Scranton, Pa., 1971.

Tsang, L., R. Brown, J. A. Kong, and G. Simmons, Numerical evaluation of electromagnetic fields due to dipole antennas in the presence of stratified media, *J. Geophys. Res.*, *29*(14), 2077–2080, 1974.

S. Barkeshli, Sabbagh Associates Inc., 4639 Morningside Drive, Bloomington, IN 47401.

P. H. Pathak, ElectroScience Laboratory, Department of Electrical Engineering, Ohio State University, Columbus, OH 43212.